ADVANCING EARTH AND SPACE SCIENCES

Geophysical Research Letters

RESEARCH LETTER
10.1029/2026GL123697

Earth's Infrared Background: A Physics-Based Null Hypothesis for the Global-Scale Subannual Variability of Outgoing Longwave Radiation

Ofer Shamir[1] and Edwin P. Gerber[1]

[1]Courant Institute of Mathematical Sciences, New York University, New York, NY, USA

Key Points:

- The Earth's Infrared Background (EIB) is defined as isotropic variability implied by the fluctuation–dissipation theorem
- The EIB is modeled using a stochastically forced energy balance climate model, yielding a red background consistent with observations
- The EIB provides a null hypothesis for separating atmospheric signals from random variability in outgoing longwave radiation

Supporting Information:

Supporting Information may be found in the online version of this article.

Correspondence to:

O. Shamir,
ofer.shamir@courant.nyu.edu

Citation:

Shamir, O., & Gerber, E. P. (2026). Earth's Infrared Background: A physics-based null hypothesis for the global-scale subannual variability of outgoing longwave radiation. *Geophysical Research Letters*, *53*, e2026GL123697. https://doi.org/10.1029/2026GL123697

Received 16 APR 2026
Accepted 26 JUN 2026

Author Contributions:

Conceptualization: Ofer Shamir, Edwin P. Gerber
Formal analysis: Ofer Shamir
Funding acquisition: Edwin P. Gerber
Investigation: Ofer Shamir
Methodology: Ofer Shamir, Edwin P. Gerber
Supervision: Edwin P. Gerber
Writing – original draft: Ofer Shamir, Edwin P. Gerber
Writing – review & editing: Ofer Shamir, Edwin P. Gerber

Abstract Much of the outgoing longwave radiation (OLR) emitted to space can be described as a noisy "background" of random variability. A rigorous characterization of this background provides an objective null spectrum and enables the isolation of atmospheric phenomena within OLR observations, such as waves and storms. Previously, the background has only been considered in the Tropics. Here we study the background on global, subannual scales and focus on its physical origins. We define the background as isotropic fluctuations implied by the fluctuation-dissipation theorem in response to internal atmospheric variability on small spatiotemporal scales. We use a stochastically forced energy balance climate model that generates a red spectrum in space and time, consistent with observations. By fitting the model to OLR measurements from satellites, we find that the background fluctuations have an upper bound of about 400 km and 2.5 days on their spatiotemporal (de)correlations, between meso-scale and synoptic-scale weather.

Plain Language Summary The infrared radiation emitted by Earth carries the "footprints" of weather and climate-related phenomena, imprinted by greenhouse gases and clouds as they interact with the radiation on its way through the atmosphere. At the same time, because of the chaotic/turbulent nature of the atmosphere, the emitted radiation also carries essentially random signals, which make up the Earth's Infrared Background. In order to accurately trace the footprints, one must also isolate the background. To this end, we follow the fluctuation–dissipation principle, according to which the random noise in a system is directly linked to how strongly the system resists disturbances. This allows us to build an empirically consistent model of the background.

1. Introduction

Only a small fraction of the outgoing longwave radiation (OLR) emitted to space, about 17% (40 out of 240 W m^{-2}, Loeb et al., 2009; Trenberth et al., 2009), originates directly at the surface. The remaining 83% only make it out to space after having been absorbed and re-emitted by greenhouse gases (about 70% of the total OLR, or 170 W m^{-2}) and clouds (about 13%, or 30 W m^{-2}). Therefore, in addition to its role in determining the global energy budget, OLR also contains the "footprints" of atmospheric variability. On subannual time scales (Figure 1a), OLR exhibits enhanced variability, relative to the global mean variance of 702 [W m^{-2}]^2, over the Intertropical Convergence Zone (Liu et al., 2020; Schneider et al., 2014), monsoonal regions, the Indian Ocean and the Maritime Continent, associated with the Madden–Julian oscillation (Jiang et al., 2020; Knutson et al., 1986; Weickmann & Khalsa, 1990; Wheeler & Hendon, 2004; Zhang, 2005), and the midlatitude storm track regions (Shaw et al., 2016). It also exhibits suppressed variability in the polar regions and in regions associated with the El Niño-Southern Oscillation (Ardanuy & Kyle, 1986; Chelliah & Arkin, 1992; Chiodi & Harrison, 2013; Fajary et al., 2019; Philander, 1983; Timmermann et al., 2018), but the latter are poorly resolved with a climatological record. Much of the observed OLR variability, however, is best described as random variability, which we term Earth's Infrared Background (EIB). To identify the footprints of atmospheric phenomena quantitatively, it is important to provide a rigorous description of the background so that an objective null hypothesis can be established.

This issue is typically encountered in the Tropics, where the identification of the tropical OLR background is essential for the quantitative analysis of equatorial waves and related coherent features (Knippertz et al., 2022). However, despite its importance, a consensual definition is still lacking, with different studies using varying approaches to estimate the background (Gehne & Kleeman, 2012; Hendon & Wheeler, 2008; Kikuchi, 2014; Kikuchi et al., 2018; Marques & Castanheira, 2018; Masunaga et al., 2006). Perhaps the most prevalent approach

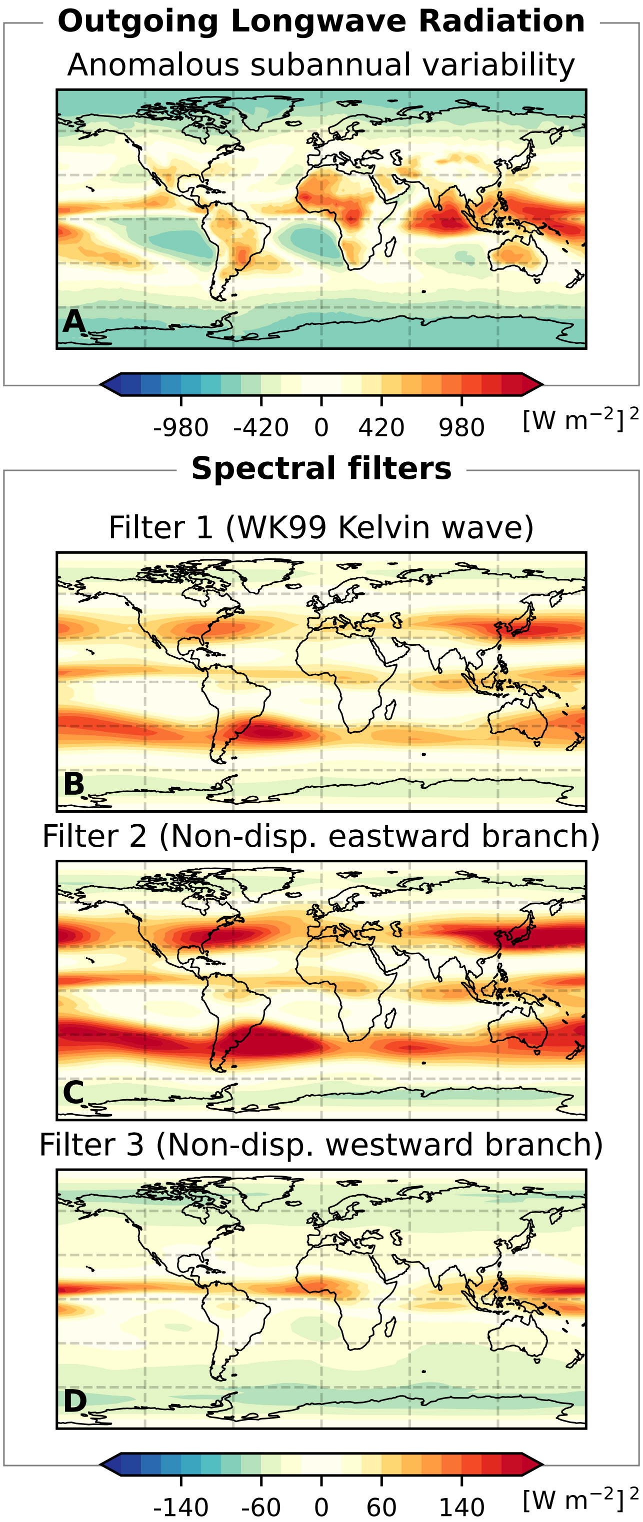

Figure 1. *The variance of outgoing longwave radiation* (*OLR*) from satellite observations during the penultimate standard climate normal (1 January 1981–31 December 2010). (a) Deviation of the subannual OLR variance from the global mean (702 [W m^{-2}]^2). (b–d) Anomalous OLR variance after filtering in spectral space using Filters 1–3 discussed in Section 4 and Figure 4f, and removing the background. Filter 1 in panel (b) corresponds in spectral space to the filter used by Wheeler and Kiladis (1999, WK99) to identify Kelvin waves, but the global application reveals eastward wave activity in the midlatitude storm tracks as well. In each panel the background variance is removed. For the full OLR in panel (a), the background is uniform and equal to the global spatial mean by construction. For the filtered OLR in panels (b–d) the background is estimated as described in Section 4.

consists of successive smoothing (Wheeler & Kiladis, 1999), which gradually redistributes the power in spectral space toward a uniform distribution, that is, leading to an asymptotically white background. Alternatively, based on the observation that the OLR has a broad red background, in the sense that its power decays with decreasing spatiotemporal scales, some studies assume a priori that the background follows a red-noise process (Hendon & Wheeler, 2008; Kikuchi, 2014; Marques & Castanheira, 2018; Masunaga et al., 2006), albeit only in time. The most relevant approach in the present context is that of stochastic modeling pioneered by Hottovy and Stechmann (2015), where the background is modeled as the response to a white noise forcing representing turbulent eddy fluxes. Standard results in stochastic climate modeling (Hasselmann, 1976; North et al., 2011) confirm that the resulting background in this approach is indeed broad sense red, a first-order process in time and second-order in space.

In this work, we consider a global OLR background on subannual time scales, and define it as isotropic variability implied by the fluctuation-dissipation theorem (FDT, Kubo, 1966) in response to the internal variability of the atmosphere. The underlying idea is that, under weak perturbations, the noise level of the system is determined by its dissipative properties and equilibrium distribution. Like classical Brownian motion, we assume a scale separation between the response and the forcing, such that the latter can be approximated as a white noise process. Unlike classical Brownian motion, however, the equilibrium distribution is not derived from first principles and is only estimated empirically. In addition, the dissipation is modeled using the "simplest" mathematical terms (Section 2), and the associated coefficients are also estimated empirically to fit observations. Although the resulting background is empirical, it meets our aim of providing an objective and quantitative null hypothesis for isolating atmospheric variability on subannual time scales. In addition, while employing a stochastic model similar to that of Hottovy and Stechmann (2015), the present approach places an additional constraint on the power spectrum of the forcing.

The assumption that the background is statistically isotropic is the spherical equivalent of statistical homogeneity in time series analysis and provides the most conservative null hypothesis for the variance. This amounts to the assumption that any anisotropy observed in the data reflects genuine physical variability rather than an artifact of the noise. We stress that the observed OLR is far from isotropic, as evident by its non-uniform variance in Figure 1a (a necessary condition for statistical isotropy). However, the identified regions of enhanced/suppressed variability in Figure 1a are associated with non-equilibrium phenomena and are the very things the null hypothesis is designed to detect.

2. A Stochastically Forced Energy Balance Climate Model ($\mathcal{E}$BCM)

A quantitative description of the background requires an empirically consistent model. The most parsimonious, lowest order, model of isotropic fluctuations that captures the above physical picture and the observed OLR variance on subannual time scales is given by the following stochastic differential equation:

$$\tau_0 \frac{\partial F}{\partial t} - \lambda_0^2 \nabla^2 F + F = S. \qquad (1)$$

Here F represents OLR fluctuations as a function of time, longitude, and latitude, and S represents a stochastic forcing due to internal fluctuations of the atmosphere. The model has a total of 3 free parameters, a time scale τ_0, which sets the temporal decorrelation, a length scale λ_0, which sets the spatial decorrelation, and an amplitude ϵ_0, which sets the variance and enters through the forcing S as described below.

This model has been extensively analyzed in the context of energy balance climate models ($\mathcal{E}$BCMs, North, 1975; North et al., 1981), where some of its applications include the study of second-order surface temperature statistics (Kim & North, 1991; North et al., 2011), and climate predictability bounds (North & Cahalan, 1981). Save for the scale-dependence of the forcing, described below, the present analysis follows these works. However, while we use a similar model, our motivation is different. In particular, we have no reason to assume that purely random OLR fluctuations are subject to Fickian diffusion. Rather, in the present context, the Laplacian on the left-hand side is the lowest order differential operator (other than the identity) that is invariant under rotation, which guarantees that the response to a statistically isotropic forcing remains isotropic (North & Cahalan, 1981; North et al., 2011), while the relaxation term guarantees that the response remains statistically stationary (Frankignoul & Hasselmann, 1977; Hasselmann, 1976). A complementary viewpoint is provided in Hottovy and

Stechmann (2015), who studied a similar model in the context of the tropical background, and suggested that it represents the effects of mean and eddy flux convergence in a turbulent atmosphere.

We take the forcing to be Gaussian white noise in time and statistically isotropic in space. The former implies that the forcing is δ-correlated in time, assuming a priori that the forcing decorrelates much faster than the response. The latter implies that the forcing is δ-correlated in Spherical Harmonic space, and depends at most on the multiple moment (Obukhov, 1947), that is,

$$\langle S_{lm}(t)S^*_{l'm'}(t')\rangle = 2\epsilon_0^2\tau_l\delta_{ll'}\delta_{mm'}\delta(t-t'), \tag{2}$$

where S_{lm} are the spectral coefficients of S of degree (total wavenumber) l and order (planetary zonal wavenumber) m, asterisks denote complex conjugates, angle brackets denote ensemble averages, sub-scripted δ_{ij} is the Kronecker delta, and argumented $\delta()$ is the Dirac delta. In a key departure from earlier works (Hottovy & Stechmann, 2015; North et al., 2011), we find it necessary to allow the forcing to be scale dependent (l dependent) to explain the observed OLR. Here $\tau_l = \tau_0/\left[1 + \lambda_0^2 l(l+1)/a^2\right]$, where a is the mean radius of the Earth, which is the only choice consistent with the FDT (Text S2 in Supporting Information S1). We note that the spatial decorrelation of the forcing is much faster than that of the resulting response (Text S3 in Supporting Information S1), so that the two are well separated in both space and time.

The process in Equation 1 is fully determined by its covariance function, which for an isotropic process depends only on the scale l and is termed angular covariance. The asymptotic angular covariance, at times much greater than the decorrelation time ($t, t' \gg \tau_l$), is (e.g., Zwanzig, 2001):

$$C_l(t,t') = \langle F_{lm}(t)F^*_{lm}(t')\rangle = \epsilon_l^2 e^{-|t-t'|/\tau_l}, \tag{3}$$

where F_{lm} are the spectral coefficients of F and $\epsilon_l = \epsilon_0\tau_l/\tau_0$. For the background spectrum, we will use the corresponding power spectral density (PSD):

$$\hat{C}_l(\omega) = 2\epsilon_l^2\tau_l/\left[\omega^2\tau_l^2 + 1\right], \tag{4}$$

where hats denote the Fourier modes in frequency domain, obtained from the covariance via the Wiener–Khinchin theorem, that is, $\hat{C}_l(\omega) = \int_{-\infty}^{\infty} C_l(\tau)e^{-i\omega\tau}d\tau$.

3. Estimating the Model Parameters From Observations

Before estimating the background, we first use Equations 3 and 4 to estimate ϵ_0, λ_0, and τ_0 from OLR measurements (Text S1 in Supporting Information S1) and discuss their physical meaning.

Consider first the angular power spectrum of the EIB (Figure 2), obtained by multiplying the time-dependent Spherical Harmonic coefficient by their complex conjugates $F_{lm}(t)F^*_{lm}(t)$ and averaging over time and m (with $|m| \leq l$) to estimate the angular variance $C_l = \langle F_{lm}F^*_{lm}\rangle$. By the Wiener-Khinchin theorem, the latter is related to the PSD via $C_l(t = t') = \int_{-\infty}^{\infty}\hat{C}_l(\omega)d\omega/2\pi$, and therefore provides a measure of the angular power spectrum in terms of the frequency-averaged PSD. At small spatial scales (large l), the $\mathcal{E}$BCM (black line) can accurately fit the raw variance (orange) by setting $t = t'$ in Equation 3 and using non-linear least squares to estimate $\epsilon_0 = 5.8 \pm 0.1$ W m^{-2} and $\lambda_0 = 384 \pm 2$ km. At large spatial scales (small l), however, there are externally forced variations and the $\mathcal{E}$BCM can only explain the observed variance on subannual time scales with frequencies above 1/360 cpd (blue). The peak at $l = 15$ is an artifact corresponding to the satellite swath half-width of about 1,250 km. A weaker imprint of the satellite swath width is also found at $l = 13$ (Text S3 in Supporting Information S1).

In the context of the stochastic model used here, λ_0 determines the spatial decorrelation of the EIB. More precisely, λ_0 provides an upper bound on the spatial decorrelation. The effective decorrelation decreases with increasing frequency (Text S3 in Supporting Information S1) and is not simply an e-folding scale (North et al., 2011). The estimated value of $\lambda_0 = 384 \pm 2$ km is well below the Nyquist wavelength of 5° in the data, consistent with random fluctuations with spatial decorrelation smaller than the smallest resolvable waves. In

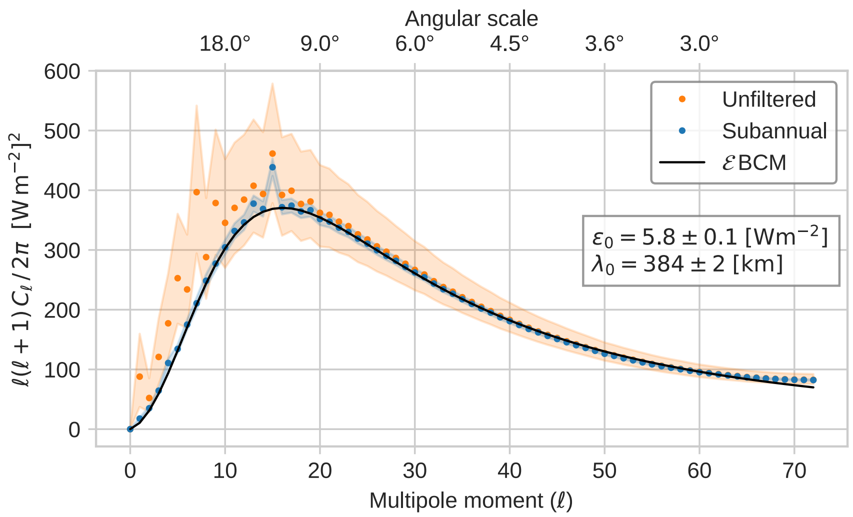

Figure 2. *The Angular power spectrum* is obtained by averaging outgoing longwave radiation fluctuations in spectral space, $F_{lm}(t)F^*_{lm}(t)$, over time and m (with $|m| \leq l$) to estimate the angular variance $C_l = \langle F_{lm} F^*_{lm} \rangle$ (orange). The angular variance provided by the $\mathcal{E}$BCM (Equation 3 with $t = t'$, black line) is fit to the data on subannual time scales (including frequencies above 1/360 cpd, blue) using nonlinear least squares to estimate ϵ_0 and λ_0. With the scaling on the ordinate, the figure represent the power per logarithmic interval in angular scale. The peak at $l = 15$ (12°) is an artifact corresponding to the satellite swath half-width of about 1,250 km. The uncertainty in the raw data is associated with the variance across m, while the uncertainty in the subseasonal data is associated with the variance across both m and the temporal windows (see Text S3 in Supporting Information S1).

addition, λ_0 is also smaller than the typical Rossby deformation radius, providing further reassurance that the background is associated with random fluctuations and suggesting that it is constrained by linear wave dynamics.

Next, consider the temporal power spectrum (Figure 3), obtained by applying a discrete Fourier transform on the time-dependent Spherical Harmonic coefficient to estimate the PSD $\tilde{F}_{lm}(\omega)\tilde{F}^*_{lm}(\omega)/\Delta\omega$, where $\Delta\omega$ is the frequency resolution, and averaging over m (with $|m| \leq l$) and l. The uptick at $\omega = 1$ cpd (the Nyquist frequency) likely includes contributions from the diurnal cycle in clouds, rainfall, and stratospheric tides, though these contributions are obscured by aliasing from higher-frequency variability. The uptick at $\omega = 0.9$ cpd (a period of 1.1 day) is associated with the satellite orbit (Wheeler & Kiladis, 1999), and the upward inflection at $\omega > 0.6$ cpd is the result of spectral leakage (Text S1 in Supporting Information S1). The dominant harmonics at $(1, 2, 3, 4)/365$ cpd (vertical dashed lines) correspond to the annual, semi-annual, and seasonal cycles, and were explicitly removed before fitting the model (Text S1 in Supporting Information S1). Having estimated ϵ_0 and λ_0 from the angular power spectrum, τ_0 can now be estimated by averaging Equation 4 over l and using non-linear least squares (black line), yielding $\tau_0 = 2.3 \pm 0.1$ days. Consistent with the angular variance in Figure 2, it is also evident in this figure that the $\mathcal{E}$BCM fits the temporal power spectrum only on subannual time scales with frequencies above 1/360 cpd.

In the context of the stochastic model used here, τ_0 provides an upper bound on the temporal decorrelation. The estimated value is similar to those obtained in the Tropics by Hendon and Wheeler (2008) assuming a red noise process in time, between 3 days at low zonal wavenumbers and 1 at high wavenumber. It is also in the ballpark of the 4 days decorrelation time used in the stochastic model of Hottovy and Stechmann (2015). While not strictly comparable, the common insight that stems from both these works in the Tropics and the present global scale analysis is that OLR decorrelates on intermediate time scales, between fast convection at small spatial scales and slower linear damping at large scales (Holton & Colton, 1972; Lin et al., 2008; Romps, 2014; Sardeshmukh & Held, 1984; Shamir et al., 2023). The effective temporal decorrelation has an l-dependent e-folding scale $\tau_l = \tau_0/\left[1 + \lambda_0^2 l(l+1)/a^2\right]$, as implied by Equation 3. At $l = 0$, the temporal decorrelation is at the lower limit of synoptic-scale weather, typically taken as 2 days. At $l = 20$ (about 1,000 km), the decorrelation is 22 hr, at the upper limit of meso-scale weather, typically taken as 1 day and 1,000 km. Finally, at $l = 72$ (about 300 km), the decorrelation is 3 hr, at the lower limit of meso-scale weather. This last value is important since, by assumption,

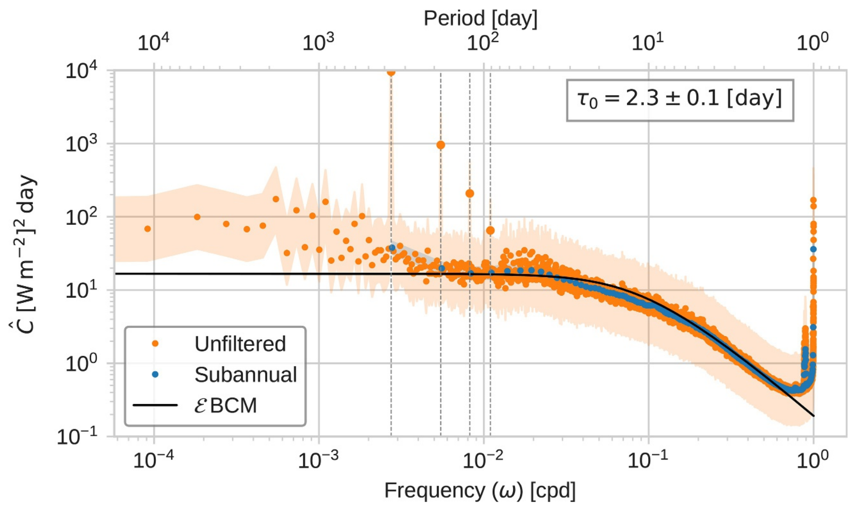

Figure 3. *The temporal power spectrum* is obtained by applying a discrete Fourier transform to the time-dependent Spherical Harmonic coefficient to estimate the power spectral density (PSD) $\tilde{F}_{lm}(\omega)\tilde{F}^*_{lm}(\omega)/\Delta\omega$, where $\Delta\omega$ is the frequency resolution, and averaging over m (with $|m| \le l$) and l (orange). The PSD provided by the $\mathcal{E}$BCM (Equation 4, black line) averaged over l is fit to the data on subannual time scales (including frequencies above 1/360 cpd, blue) using the values of ϵ_0 and λ_0 estimated in Figure 2, and nonlinear least squares to estimate τ_0. The figure represents the power per frequency. Vertical dashed lines indicate the annual cycle at 1/365 cpd and subsequent three harmonics: $(2,3,4)/365$ cpd. The uncertainty in the raw data is associated with the variance across m, while the uncertainty in the subseasonal data is associated with the variance across both m and the temporal windows.

the temporal correlation of the forcing is much shorter than that of the response. Therefore, the forcing mechanism (s) must decorrelate faster than meso-scale weather, to allow for sufficient scale separation between the two.

4. Estimating the Background Spectrum and Filtering in Spectral Space

The full description of the EIB consists of its joint power distribution in ω, l, m space. We consider the PSD obtained by first applying a discrete Fourier transform to the time-dependent Spherical Harmonic coefficients to estimate $\tilde{F}_{lm}(\omega)\tilde{F}^*_{lm}(\omega)/\Delta\omega$, and then averaging over m (with $|m| \le l$) or l (with $|m| \le l \le 72$) to obtain the PSD as a function of ω and l (Figure 4, top row) or ω and m (Figure 4, bottom row), respectively. For the latter, the background (Figure 4e) depends on m implicitly through the m-dependent averaging, although the $\mathcal{E}$BCM does not.

Having estimated the model parameters, we generate a random realization of the background (Figures 4b and 4e) by solving the spectral space version of Equation 1 as an l-dependent Ornstein–Uhlenbeck process (Text S1 in Supporting Information S1), having the same sample size and sample rate as the observed OLR. The advantage of this approach is that the realized background accounts for the effects of finite sampling, therefore providing a better basis for comparison than the analytic PSD (black contours) given by Equation 4. Significant signals (Figures 4c and 4f) are then identified as ω, l, m combinations where the ratio of observed to realized PSDs is significantly different from one (see Text S1 in Supporting Information S1 for statistical analysis). In other words, the null hypothesis is that the power follows a red-noise distribution in both space and time, and the alternative hypothesis is that it differs.

Aside from satellite artifacts (black rectangles) and spectral leakage at high frequencies (above 0.8 cpd, see also Text S1 in Supporting Information S1), the global background reveals distinct regions of significance in Figure 4f. In order to relate these regions to known atmospheric variability, at least in part, we examine below the resulting spatial variance after filtering in spectral space according to these regions. The chosen filters are outlined by black (pseudo-) triangles and labeled 1–6. While the background is isotropic by definition, the application of the filters introduces anisotropies. Therefore, the filters were applied to both the observed OLR and the realized background, and their spatial variance were subtracted.

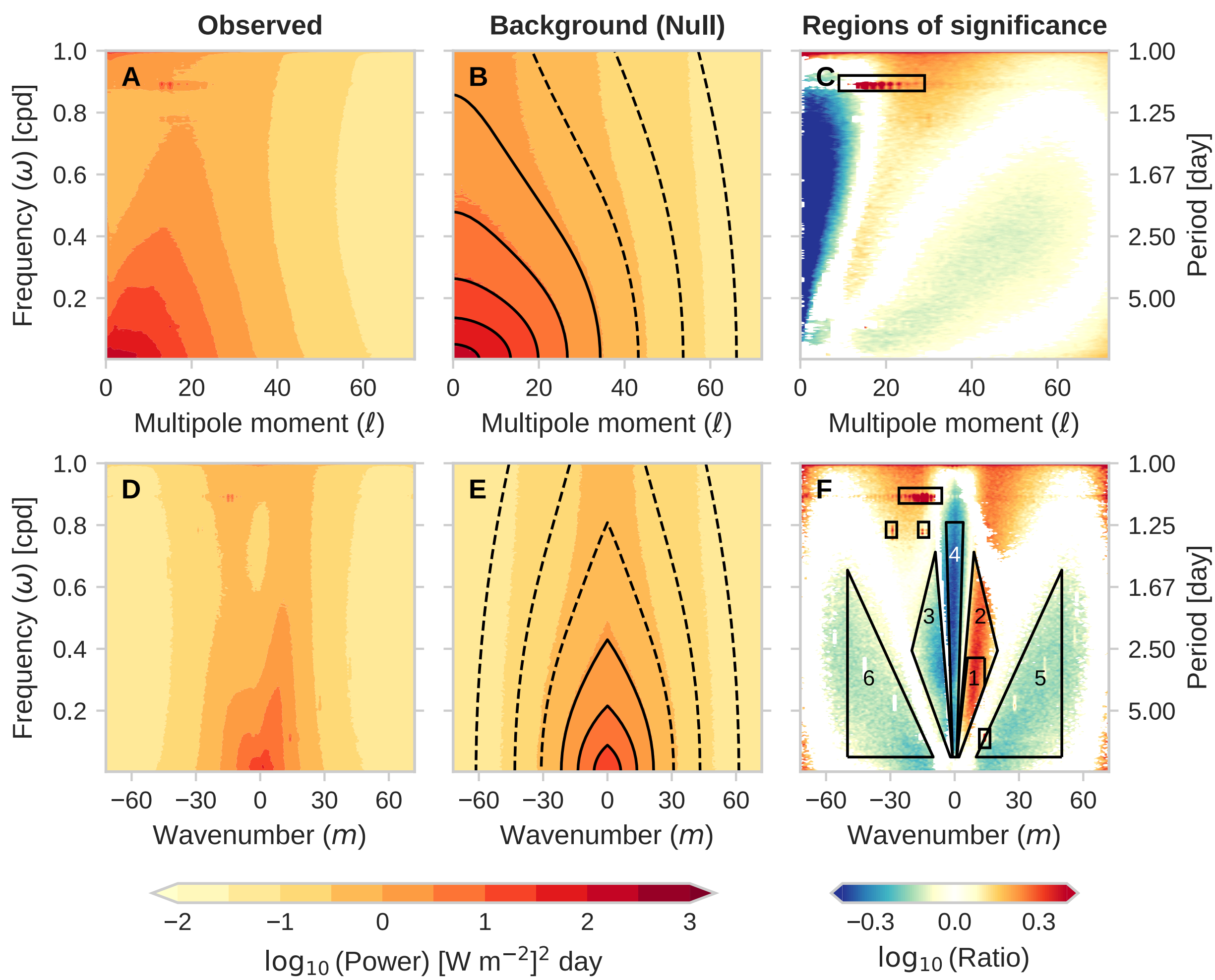

Figure 4. *Space-time spectra*. The power spectral density (PSD) of the observed outgoing longwave radiation are obtained by averaging $\tilde{F}_{lm}(\omega)\tilde{F}^*_{lm}(\omega)/\Delta\omega$, where tildes denote the Discrete Fourier Transform and $\Delta\omega$ is the frequency resolution, over (a) zonal wavenumber m and (d) total wavenumber l with $|m| \leq l$. (b, e) The corresponding PSD of a random realization of the background, generated by solving the spectral space version of Equation 1 as an l-dependent Ornstein–Uhlenbeck process (Text S1 in Supporting Information S1), and having the same sample size and sample rate as in the observations (a, d). For comparison, black contours mark the analytic PSD given by Equation 4, highlighting uncertainty associated with finite sampling. (c, f) Regions of significance, where the ratio of observed to background PSD is significantly different from 1 (Text S1 in Supporting Information S1). With the logarithmic scaling, the power in panel (c), (f) is simply the difference between the spectra in panels (a, b), (d, e). The spectral filters used in Figures 1b–1d and in Text S3 in Supporting Information S1 are outlined in panel (f) and labeled 1–6. Black rectangles in panels (c, f) indicate satellite artifacts.

For comparison, Filter 1 corresponds to the exact region of spectral space used in Wheeler and Kiladis (1999) to filter Kelvin waves in the Tropics, but it is applied to the global subannual variability rather than only equatorially symmetric seasonal variability. The resulting spatial variance is shown in Figure 1b. Variability associated with equatorial Kelvin waves can indeed be identified in the Tropics. However, when applied globally, the variance corresponding to this region of spectral space also captures variability in the midlatitude storm track regions, which is closely associated with midlatitude baroclinic Rossby waves (Shaw et al., 2016).

Filter 1 makes up part of a larger region of significance identified in Figure 4f and delineated by Filter 2, which represents non-dispersive eastward propagating variability. The resulting spatial variance (Figure 1c) is generally similar to that of Filter 1, but with stronger variability consistent with the larger area in spectral space, which is, in turn, consistent with the broader spectrum of midlatitude baroclinic Rossby waves toward smaller scales and higher frequencies.

Filter 3 is a mirror image of Filter 2 about wavenumber 0 and represents non-dispersive, westward propagating variability. The variability in the midlatitude storm track regions is clearly suppressed compared to the eastward propagating branch in Filter 2 (Figure 1d), and the polar regions are also suppressed compared to the background.

10.1029/2026GL123697

Enhanced spatial variance is focused only in the Tropics. Its spatial pattern bears some resemblance to that of the westward propagating equatorial Rossby wave (e.g., Wheeler & Kiladis, 1999, see also Text S3 in Supporting Information S1), despite covering a different region of spectral space. Even in the Tropics, it exhibits less variability than Filter 2, despite covering an area of the same size in spectral space.

Together, the picture that stems from Filters 2 and 3 is consistent with traditional midlatitude Rossby wave dynamics, not just in terms of spatiotemporal scales and geographical projection, but also in dynamical terms. The enhanced variability of the eastward branch and the suppressed variability of the westward branch are consistent with Doppler shifting by the mean winds of the extratropical jets. From this perspective, the remanent tropical pattern in Filter 3 is consistent with the weak easterly mean winds in that region. Moreover, the fact that this variability appears as non-dispersive waves in spectral space is consistent with the dispersion relation of Rossby waves in the limit of large wavelengths compared to the Rossby radius of deformation.

Consistent with large spatial scales centered around wavenumber 0, the spatial variance corresponding to Filter 4 (Text S3 in Supporting Information S1) consists of zonally symmetric equator-to-pole gradient, highlighting the lower OLR variability at the poles observed in Figure 1a. Finally, the spatial variance corresponding to Filters 5 and 6 (Text S3 in Supporting Information S1) highlights regional variability in the monsoonal regions and the ITCZ, in addition to the storm track regions. Additional filters are considered in Text S3 in Supporting Information S1 to motivate further analysis beyond the scope of this work.

5. Conclusions and Discussion

We define the EIB as isotropic, random fluctuations implied by the FDT, in response to internal variability of the atmosphere on small spatiotemporal scales. A simple stochastically forced energy balance climate model is capable of explaining the observed space/time spectra on subannual time scales, provided the forcing has scale dependence. The resulting (joint) space-time spectrum of the background captures the total observed variance, by construction, and is distributed in space and time according to a red noise process. The deviations from this red background reveal some atmospheric variability of interest, including equatorial Kelvin waves, midlatitude Rossby waves, monsoonal circulation, and the large-scale meridional circulation.

As defined here and in previous work, the background captures the same total variance as the raw data. This widely adopted terminology has led to confusion and criticism, as the word background implies a baseline level. Semantically, it is reasonable to expect a lower bound. While we have adopted the preceding terminology, a more accurate term to describe the target of our analysis would be a "null spectrum," which need not be a lower bound. It is based on the null hypothesis that there is no spatiotemporal structure in the data. By construction, it captures the total observed variance, but is distributed in space and time according to an idealized red noise process. Therefore, it is the distribution of power in spectral space, not the total power, that distinguishes the observed OLR from the background and enables the identification of significant signals.

If the background is restricted to be a lower bound, it implicitly assumes that significant signals consist only of enhanced variability. In contrast, from the point of view of a random null hypothesis, both enhanced and suppressed variability are possible. Physically, the variability at certain wavenumbers and frequencies can be suppressed due to anti-resonance. In the Tropics, for example, OLR was found to be suppressed as a result of anti-resonance between (dry) wave modes and (moist) convection (Stechmann & Hottovy, 2017). On a global scale (the present work), suppressed variability in the non-dispersive westward branch is important for completing the physical picture of the midlatitude Rossby wave dynamics in the presence of westerly jets.

An important limitation of our null spectrum that should be kept in mind when interpreting the results is the effects of spatial variations in the time mean wind. In the Tropics, for example, the PSD of convectively coupled equatorial waves was found to be systematically modulated as a result of Doppler shifting by the varying mean wind in different tropical sectors (Dias & Kiladis, 2014). Moreover, much of the spread in spectral space (interpreted as a spread in the "equivalent depth") was attributed to this effect. It is thus possible that the regions of significance identified in the present work are "smeared out" by the varying mean wind across the globe. Nonetheless, the EIB reveals distinct regions of variability in spectral space associated with the dynamics of the atmosphere.

Finally, some more interesting questions remain. Although grounded in the fundamental principle of the FDT, the forcing and damping terms were chosen for simplicity and empirical agreement, rather than derived from first principles. The question is therefore what are the relevant physical processes at play. A related question is what determines the (de)correlation scales of the background.

Conflict of Interest

The authors declare no conflicts of interest relevant to this study.

Availability Statement

NOAA Interpolated outgoing longwave radiation data provided by the NOAA PSL, Boulder, Colorado, USA, is publicly available on their website at https://psl.noaa.gov/data/gridded/data.olrcdr.interp.html. The code to reproduce the analysis and figures is available at https://github.com/ofershamir/earth-infrared-background.

Acknowledgments

We thank 2 anonymous reviewers for their helpful comments on an earlier version. O. S. and E. P. G. were supported by Schmidt Sciences LLC. E. P. G. was also supported by the National Science Foundation through Award OAC-2004572. We also acknowledge high-performance computing support from New York University and the Derecho system (doi: 10.5065/qx9a-pg09) and the Cheyenne system (doi: 10.5065/D6RX99HX) provided by the National Center for Atmospheric Research (NCAR), sponsored by the National Science Foundation.

References

Ardanuy, P. E., & Kyle, H. L. (1986). El Nino and outgoing longwave radiation: Observations from Nimbus-7 ERB. *Monthly Weather Review*, *114*(2), 415–433. https://doi.org/10.1175/1520-0493(1986)114<0415:enaolr>2.0.co;2

Chelliah, M., & Arkin, P. (1992). Large-scale interannual variability of monthly outgoing longwave radiation anomalies over the global tropics. *Journal of Climate*, *5*(4), 371–389. https://doi.org/10.1175/1520-0442(1992)005<0371:lsivom>2.0.co;2

Chiodi, A. M., & Harrison, D. E. (2013). El Niño impacts on seasonal US atmospheric circulation, temperature, and precipitation anomalies: The OLR-event perspective. *Journal of Climate*, *26*(3), 822–837. https://doi.org/10.1175/jcli-d-12-00097.1

Dias, J., & Kiladis, G. N. (2014). Influence of the basic state zonal flow on convectively coupled equatorial waves. *Geophysical Research Letters*, *41*(19), 6904–6913. https://doi.org/10.1002/2014gl061476

Fajary, F. R., Hadi, T. W., & Yoden, S. (2019). Contributing factors to spatiotemporal variations of outgoing longwave radiation (OLR) in the tropics. *Journal of Climate*, *32*(15), 4621–4640. https://doi.org/10.1175/jcli-d-18-0350.1

Frankignoul, C., & Hasselmann, K. (1977). Stochastic climate models, part II Application to sea-surface temperature anomalies and thermocline variability. *Tellus*, *29*(4), 289–305. https://doi.org/10.3402/tellusa.v29i4.11362

Gehne, M., & Kleeman, R. (2012). Spectral analysis of tropical atmospheric dynamical variables using a linear shallow-water modal decomposition. *Journal of the Atmospheric Sciences*, *69*(7), 2300–2316. https://doi.org/10.1175/jas-d-10-05008.1

Hasselmann, K. (1976). Stochastic climate models part I. Theory. *Tellus*, *28*(6), 473–485. https://doi.org/10.3402/tellusa.v28i6.11316

Hendon, H. H., & Wheeler, M. C. (2008). Some space–time spectral analyses of tropical convection and planetary-scale waves. *Journal of the Atmospheric Sciences*, *65*(9), 2936–2948. https://doi.org/10.1175/2008jas2675.1

Holton, J. R., & Colton, D. E. (1972). A diagnostic study of the vorticity balance at 200 mb in the tropics during the northern summer. *Journal of the Atmospheric Sciences*, *29*(6), 1124–1128. https://doi.org/10.1175/1520-0469(1972)029<1124:adsotv>2.0.co;2

Hottovy, S., & Stechmann, S. N. (2015). A spatiotemporal stochastic model for tropical precipitation and water vapor dynamics. *Journal of the Atmospheric Sciences*, *72*(12), 4721–4738. https://doi.org/10.1175/jas-d-15-0119.1

Jiang, X., Adames, Á. F., Kim, D., Maloney, E. D., Lin, H., Kim, H., et al. (2020). Fifty years of research on the Madden-Julian Oscillation: Recent progress, challenges, and perspectives. *Journal of Geophysical Research: Atmospheres*, *125*(17), e2019JD030911. https://doi.org/10.1029/2019jd030911

Kikuchi, K. (2014). An introduction to combined Fourier–wavelet transform and its application to convectively coupled equatorial waves. *Climate Dynamics*, *43*(5), 1339–1356. https://doi.org/10.1007/s00382-013-1949-8

Kikuchi, K., Kiladis, G. N., Dias, J., & Nasuno, T. (2018). Convectively coupled equatorial waves within the MJO during CINDY/DYNAMO: Slow kelvin waves as building blocks. *Climate Dynamics*, *50*(11), 4211–4230. https://doi.org/10.1007/s00382-017-3869-5

Kim, K.-Y., & North, G. R. (1991). Surface temperature fluctuations in a stochastic climate model. *Journal of Geophysical Research*, *96*(D10), 18573–18580. https://doi.org/10.1029/91jd01959

Knippertz, P., Gehne, M., Kiladis, G. N., Kikuchi, K., Rasheeda Satheesh, A., Roundy, P. E., et al. (2022). The intricacies of identifying equatorial waves. *Quarterly Journal of the Royal Meteorological Society*, *148*(747), 2814–2852. https://doi.org/10.1002/qj.4338

Knutson, T. R., Weickmann, K. M., & Kutzbach, J. E. (1986). Global-scale intraseasonal oscillations of outgoing longwave radiation and 250 mb zonal wind during Northern Hemisphere summer. *Monthly Weather Review*, *114*(3), 605–623. https://doi.org/10.1175/1520-0493(1986)114<0605:gsiooo>2.0.co;2

Kubo, R. (1966). The fluctuation-dissipation theorem. *Reports on Progress in Physics*, *29*(1), 255–284. https://doi.org/10.1088/0034-4885/29/1/306

Lin, J., Mapes, B. E., & Han, W. (2008). What are the sources of mechanical damping in Matsuno–Gill-type models? *Journal of Climate*, *21*(2), 165–179. https://doi.org/10.1175/2007jcli1546.1

Liu, C., Liao, X., Qiu, J., Yang, Y., Feng, X., Allan, R. P., et al. (2020). Observed variability of intertropical convergence zone over 1998—2018. *Environmental Research Letters*, *15*(10), 104011. https://doi.org/10.1088/1748-9326/aba033

Loeb, N. G., Wielicki, B. A., Doelling, D. R., Smith, G. L., Keyes, D. F., Kato, S., et al. (2009). Toward optimal closure of the Earth's top-of-atmosphere radiation budget. *Journal of Climate*, *22*(3), 748–766. https://doi.org/10.1175/2008jcli2637.1

Marques, C. A., & Castanheira, J. M. (2018). Diagnosis of free and convectively coupled equatorial waves. *Mathematical Geosciences*, *50*(5), 585–606. https://doi.org/10.1007/s11004-018-9729-y

Masunaga, H., L'Ecuyer, T. S., & Kummerow, C. D. (2006). The Madden–Julian Oscillation recorded in early observations from the tropical rainfall measuring mission (TRMM). *Journal of the Atmospheric Sciences*, *63*(11), 2777–2794. https://doi.org/10.1175/jas3783.1

North, G. R. (1975). Theory of energy-balance climate models. *Journal of the Atmospheric Sciences*, *32*(11), 2033–2043. https://doi.org/10.1175/1520-0469(1975)032<2033:toebcm>2.0.co;2

North, G. R., & Jr.Cahalan, R. F. (1981). Predictability in a solvable stochastic climate model. *Journal of the Atmospheric Sciences*, *38*(3), 504–513. https://doi.org/10.1175/1520-0469(1981)038<0504:piassc>2.0.co;2

North, G. R., Cahalan, R. F., & Coakley, J. A. (1981). Energy balance climate models. *Reviews of Geophysics*, *19*(1), 91–121. https://doi.org/10.1029/rg019i001p00091

North, G. R., Wang, J., & Genton, M. G. (2011). Correlation models for temperature fields. *Journal of Climate*, *24*(22), 5850–5862. https://doi.org/10.1175/2011jcli4199.1

Obukhov, A. M. (1947). Statistically homogeneous fields on a sphere. *Usp. Mat. Nauk*, *2*(2), 196–198.

Philander, S. G. H. (1983). El Niño southern oscillation phenomena. *Nature*, *302*(5906), 295–301. https://doi.org/10.1038/302295a0

Romps, D. M. (2014). Rayleigh damping in the free troposphere. *Journal of the Atmospheric Sciences*, *71*(2), 553–565. https://doi.org/10.1175/jas-d-13-062.1

Sardeshmukh, P. D., & Held, I. M. (1984). The vorticity balance in the tropical upper troposphere of a general circulation model. *Journal of the Atmospheric Sciences*, *41*(5), 768–778. https://doi.org/10.1175/1520-0469(1984)041<0768:tvbitt>2.0.co;2

Schneider, T., Bischoff, T., & Haug, G. H. (2014). Migrations and dynamics of the intertropical convergence zone. *Nature*, *513*(7516), 45–53. https://doi.org/10.1038/nature13636

Shamir, O., Garfinkel, C. I., Gerber, E. P., & Paldor, N. (2023). The Matsuno–Gill model on the sphere. *Journal of Fluid Mechanics*, *964*, A32. https://doi.org/10.1017/jfm.2023.369

Shaw, T., Baldwin, M., Barnes, E. A., Caballero, R., Garfinkel, C., Hwang, Y.-T., et al. (2016). Storm track processes and the opposing influences of climate change. *Nature Geoscience*, *9*(9), 656–664. https://doi.org/10.1038/ngeo2783

Stechmann, S. N., & Hottovy, S. (2017). Unified spectrum of tropical rainfall and waves in a simple stochastic model. *Geophysical Research Letters*, *44*(20), 10–713. https://doi.org/10.1002/2017gl075754

Timmermann, A., An, S.-I., Kug, J.-S., Jin, F.-F., Cai, W., Capotondi, A., et al. (2018). El Niño–southern oscillation complexity. *Nature*, *559*(7715), 535–545. https://doi.org/10.1038/s41586-018-0252-6

Trenberth, K. E., Fasullo, J. T., & Kiehl, J. (2009). Earth's global energy budget. *Bulletin of the American Meteorological Society*, *90*(3), 311–324. https://doi.org/10.1175/2008BAMS2634.1

Weickmann, K., & Khalsa, S. (1990). The shift of convection from the Indian Ocean to the western Pacific Ocean during a 30–60 day oscillation. *Monthly Weather Review*, *118*(4), 964–978. https://doi.org/10.1175/1520-0493(1990)118<0964:tsocft>2.0.co;2

Wheeler, M. C., & Hendon, H. H. (2004). An all-season real-time multivariate MJO index: Development of an index for monitoring and prediction. *Monthly Weather Review*, *132*(8), 1917–1932. https://doi.org/10.1175/1520-0493(2004)132<1917:aarmmi>2.0.co;2

Wheeler, M. C., & Kiladis, G. N. (1999). Convectively coupled equatorial waves: Analysis of clouds and temperature in the wavenumber–frequency domain. *Journal of the Atmospheric Sciences*, *56*(3), 374–399. https://doi.org/10.1175/1520-0469(1999)056<0374:ccewao>2.0.co;2

Zhang, C. (2005). Madden-Julian oscillation. *Reviews of Geophysics*, *43*(2), RG2003. https://doi.org/10.1029/2004rg000158

Zwanzig, R. (2001). *Nonequilibrium statistical mechanics*. Oxford University Press.

References From the Supporting Information

Arguez, A., & Vose, R. S. (2011). The definition of the standard WMO climate normal: The key to deriving alternative climate normals. *Bulletin of the American Meteorological Society*, *92*(6), 699–704. https://doi.org/10.1175/2010bams2955.1

Liebmann, B., & Smith, C. A. (1996). Description of a complete (interpolated) outgoing longwave radiation dataset. *Bulletin of the American Meteorological Society*, *77*(6), 1275–1277.

Milly, P. C., Betancourt, J., Falkenmark, M., Hirsch, R. M., Kundzewicz, Z. W., Lettenmaier, D. P., & Stouffer, R. J. (2008). Stationarity is dead: Whither water management? *Science*, *319*(5863), 573–574. https://doi.org/10.1126/science.1151915

Mudelsee, M. (2010). *Climate time series analysis*. Springer.

Percival, D. B., & Walden, A. T. (1993). *Spectral analysis for physical applications*. Cambridge University Press.

Wieczorek, M. A., & Meschede, M. (2018). SHTools: Tools for working with spherical harmonics. *Geochemistry, Geophysics, Geosystems*, *19*(8), 2574–2592. https://doi.org/10.1029/2018gc007529